geosciences

MDPI

Article

Fracture Kinematics and Holocene Stress Field at the Krafla Rift, Northern Iceland

Noemi Corti [1], Fabio L. Bonali [1,2], Federico Pasquaré Mariotto [3,*], Alessandro Tibaldi [1,2], Elena Russo [1,2], Ásta Rut Hjartardóttir [4], Páll Einarsson [4], Valentina Rigoni [1] and Sofia Bressan [1]

1 Department of Earth and Environmental Sciences, University of Milan-Bicocca, 20126 Milan, Italy; n.corti3@campus.unimib.it (N.C.); fabio.bonali@unimib.it (F.L.B.); alessandro.tibaldi@unimib.it (A.T.); e.russo11@campus.unimib.it (E.R.); v.rigoni@campus.unimib.it (V.R.); s.bressan2@campus.unimib.it (S.B.)
2 CRUST-Interuniversity Center for 3D Seismotectonics with Territorial Applications, 66100 Chieti Scalo, Italy
3 Department of Human and Innovation Sciences, Insubria University, 21100 Varese, Italy
4 Nordic Volcanological Center, Institute of Earth Sciences, University of Iceland, IS-102 Reykjavík, Iceland; astahj@hi.is (Á.R.H.); palli@hi.is (P.E.)
* Correspondence: pas.mariotto@uninsubria.it

Abstract: In the Northern Volcanic Zone of Iceland, the geometry, kinematics and offset amount of the structures that form the active Krafla Rift were studied. This rift is composed of a central volcano and a swarm of extension fractures, normal faults and eruptive fissures, which were mapped and analysed through remote sensing and field techniques. In three areas, across the northern, central and southern part of the rift, detailed measurements were collected by extensive field surveys along the post-Late Glacial Maximum (LGM) extension fractures and normal faults, to reconstruct their strike, opening direction and dilation amount. The geometry and the distribution of all the studied structures suggest a northward propagation of the rift, and an interaction with the Húsavík–Flatey Fault. Although the opening direction at the extension fractures is mostly normal to the general N–S rift orientation (average value N99.5° E), a systematic occurrence of subordinate transcurrent components of motion is noticed. From the measured throw at each normal fault, the heave was calculated, and it was summed together with the net dilation measured at the extension fractures; this has allowed us to assess the stretch ratio of the rift, obtaining a value of 1.003 in the central sector, and 1.001 and 1.002 in the northern and southern part, respectively.

Keywords: extension fracture; rift; Krafla; stresses; Iceland

Citation: Corti, N.; Bonali, F.L.; Pasquaré Mariotto, F.; Tibaldi, A.; Russo, E.; Hjartardóttir, Á.R.; Einarsson, P.; Rigoni, V.; Bressan, S. Fracture Kinematics and Holocene Stress Field at the Krafla Rift, Northern Iceland. *Geosciences* **2021**, *11*, 101. https://doi.org/10.3390/geosciences11020101

Academic Editors: Jesus Martinez-Frias and Karoly Nemeth

Received: 20 January 2021
Accepted: 15 February 2021
Published: 20 February 2021

1. Introduction

The Northern Volcanic Zone (NVZ) of Iceland represents the emergence of the Mid-Atlantic Ridge and is composed of five parallel rift zones (Figure 1) that are, from west to east, the Theistareykir, Krafla, Fremrinámar, Askja and Kverkfjöll rifts [1]. Although much research has been focused on the Krafla system [1–4], the most detailed studies on rift kinematics and geometry have been carried out at the Theistareykir rift [5–10]. These works show a complex pattern of kinematics with the presence of transcurrent components of motions that, in particular, become systematic in the northern section of the Theistareykir rift, the Theistareykir Fissure Swarm (ThFS), where a right-lateral component is observed. This has been suggested to be generated by a heterogeneous simple shear with a smoothly increasing strain gradient produced by the WNW–ESE Grimsey Lineament right-lateral shear zone (GRL in Figure 1b) [7].

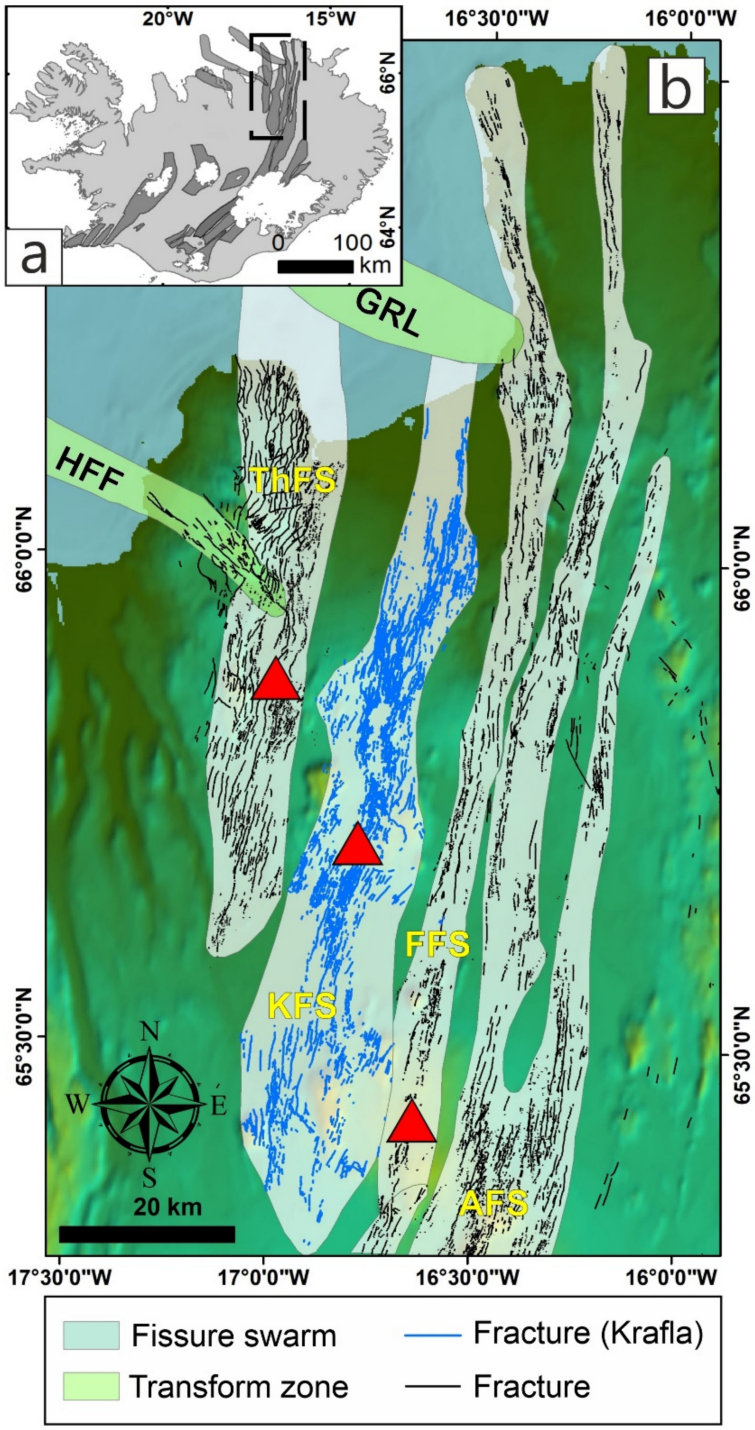

Figure 1. (**a**) Volcanic systems of Iceland, with the main volcano-tectonic rift zones of Iceland (darker grey areas, after Einarsson and Saemundsson [11]; Hjartardóttir et al. [1]): the black rectangle indicates the Northern Volcanic Zone (NVZ); (**b**) Map of the NVZ with all the structures and central volcanoes. Light green areas represent the transform zones, whereas light blue areas represent the fissure swarms of the region, where all the structures are shown (after Magnúsdóttir and Brandsdóttir [12]; Hjartardóttir et al. [1,13]); the KFS structures are highlighted in blue. AFS: Askja Fissure Swarm; FFS: Fremrinamar Fissure Swarm; HFF: Husavik Flatey Fault; GRL: Grimsey Lineament; KFS: Krafla Fissure Swarm; ThFS: Theistareykir Fissure Swarm.

Another important feature found at the ThFS is the greater development of normal faults and tension fractures north of its central volcano than in its southern portion. South

of the central volcano, in fact, Holocene faults and tension fractures are less developed in terms of slip, length and number. This asymmetric development of the rift has been interpreted by Tibaldi et al. [6] as the effect of buttressing induced by another major volcano and its magma feeding system located just east of the southern ThFS, corresponding to the Krafla volcano [14] (Figure 1b), and by the fact that the Krafla rift approaches the ThFS southwards [15], thus contributing to an increase in buttressing induced by repeated dyke injection along the Krafla rift, or Krafla Fissure Swarm (KFS). Based on these observations, the study of the Theistareykir Fissure Swarm and of the Grimsey Lineament suggested that a rift termination can interact with a transversal shear zone, whereas the study of the asymmetric development of the ThFS suggested possible interactions with the KFS. These hypotheses are worth further investigation through an in-depth analysis of the architecture and kinematics of the KFS, which is a major, 100-km-long structure. Moreover, quantifying the spreading direction across a rift zone is of paramount importance for several practical applications, ranging from the assessment of seismic hazard [16] to the evaluation of factors that can contribute to magma uprising, and thus to the assessment of volcanic hazard [17]. However, the precise definition of the possible variation in the spreading direction along a rift requires the knowledge of a series of parameters that include the architecture of the rift, the geometry of each single fault and extension fracture, the timing of the rifting and the kinematics; needless to say, the quality of the collected data must be as good as possible. The most detailed reconstruction of the strain field can be achieved only by collecting a huge amount of horizontal dilation values. In view of the above, we set about analysing, with the greatest possible detail, the geometry and kinematics of the normal faults and extension fractures that characterize the Krafla rift. Here, we present the results of a survey conducted through remote sensing techniques along the whole rift, as well as field surveys in three areas located in the northern, central and southern part of the rift.

Our work on one hand is a contribution to a better understanding of this important seismogenic and volcanic rift, and on the other hand is of more general interest, as it allows for a better understanding of the processes that take place in regions under extension. Moreover, it sheds new light on the mechanisms of plate separation and enables investigating how rifts can interact. Furthermore, our study is of interest to understand the interaction of a transform fault with a rift and can contribute to increasing knowledge about oceanic ridges. The KFS is extremely suitable for such studies because (i) the region is almost unvegetated due to harsh climate conditions; (ii) deformation rates are high, of the order of 17–18 mm/year across the whole Northern Volcanic Zone [18,19]; and (iii) the rocks affected by faulting and fracturing mainly belong to recent deposits (Holocene-historic), so that the effects of erosion are not meaningful, and the structures show preserved features.

2. Geological and Tectonic Background

Iceland is a 300 × 500 km platform located in the Northern Atlantic Ocean, at the junction between the Kolbeinsey Ridge in the north and the Reykjanes Ridge in the south [20]. Its location makes it a unique site for geology, since it is situated both along a divergent plate boundary (between the Eurasian and American plates) and on top of a hotspot [21]. From a geological point of view, Iceland is characterized by the widespread presence of Neogene and Pleistocene basalts, bordering the active rift systems that cut through the island from SW to NNE. Such active rifts are made of swarms of faults, extension fractures and basaltic volcanoes, and are marked by the occurrence of eruptions, representing the surface expression of the mid-ocean ridge [20]. Their formation is due to plate-pull associated with mid-oceanic ridge activity and magma upwelling. Thus, Iceland is the result of the combination of hot spot and mid-ocean ridge magmatism [21–24]. Nowadays, there are 30, presently active, 40–150 km long and 5–20 km wide volcanic systems, all hosting a central volcanic edifice [20]. The spreading direction, holding the North America Plate fixed, is given with a plate velocity vector of 18.2 mm/year in a direction of 105° for Central Iceland [21].

This spreading process, in the northern part of the island, is accommodated by the NVZ, the northern part of which joins with the offshore Tjörnes Fracture Zone. This is made of three WNW-oriented transform areas: the Húsavík transform fault (or the Húsavík–Flatey Fault, HFF), the Grímsey oblique rift (or Grimsey Lineament, GRL) and the Dalvík zone [21,25–28]. The center of the Icelandic hotspot is situated in the southern sector of the NVZ [29]. As mentioned above, the NVZ consists of five volcanic systems, which are volcano-tectonic rift zones [1,30] (Figure 1) composed of swarms of normal faults, extension fractures and eruptive fissures, as well as a main central volcano [25]. The trend of the 5–20 km-wide and 60–100 km-long rift zones is N–S to NNE–SSW. The KFS is the second westernmost rift of the NVZ, and is made of the Krafla active central volcano, normal faults and extension fractures, as well as numerous eruptive fissures that stretch north and south of the volcano. These structures cut Pleistocene and, mostly, post-Late Glacial Maximum (LGM) deposits emplaced since ~12,000 years BP [31]. All structures are mostly N to NNE oriented and have been the site of volcano-tectonic deformation for the last 100 ka [1,13,14,32,33]. The Krafla central volcano is marked by a major caldera (about 8 km wide) that is thought to have formed during a large ignimbrite-forming eruption about 110 ka ago [33,34]. After caldera formation, it has widened about 2 km in an E–W direction as a consequence of plate spreading [33]. Although the Krafla volcano is mainly basaltic, silicic deposits can be found near the caldera [33,35]. Below the volcano, a magma chamber of irregular form is located: its top lies at a depth of 3 km and its bottom is situated above 7 km depth [36]. Ground deformation [37] and geochemical data [38] suggest that, below this main magma chamber, deeper magma reservoirs may occur.

Within the NVZ, major rifting episodes were observed, respectively, in 1618 at the ThFS, in 1724–1729 at the KFS and in 1874–1876 at the Askja volcanic system [39]. In 2014, a dyke intrusion from the Bárðarbunga volcano migrated northward, affecting the NVZ [40,41]. One of the most recent rifting activity in the NVZ has taken place within the KFS and its central volcano. Two rifting episodes have occurred here in the last 1140 years: the 1724–1729 "Mývatn fires episode" and the instrumentally recorded 1975–1984 Krafla rifting episode. During both episodes, intense earthquake activity and fault displacements (often with graben subsidence) took place within the fissure swarm. Rifting processes were accompanied by fissure eruptions [33,42]. The volcano-tectonic processes that took place in the KFS from 1975 to 1984 [39,43,44] were marked by about 20 rifting events and nine lava eruptions. During each rifting event, magma escaped from the chamber below the Krafla volcano and intruded in the form of dykes [45]. These typically propagated to the surface in the caldera area and to a depth of about 3 km at the northernmost end of the KFS [46]. During these events, rapid subsidence within the Krafla volcano was instrumentally documented, followed by earthquake swarms directed away from the caldera and into the fissure swarm. All the above was associated with graben subsidence in the respective section of the fissure swarm and sometimes with eruptions near the caldera. [43,47]. Although the 2-cm-yr spreading rate proceeds in a constant manner [48], the spreading that is observed at individual fissure swarms, such as the KFS, is episodic [49,50]. This is because the fractures within the fissure swarms are mainly activated during rifting episodes, when dykes intrude along fissure swarms, often triggering fissure eruptions [49,51].

With regard to the spreading direction in the whole NVZ, Drouin et al. [18] measured a value of N112° E, for a limited time window of 4 years and based only on GPS data. Two other works, on the basis of GPS data and focusing on the 1997–2011 and 2006–2010 time intervals, provide values of N109° E and N115° E, respectively, for the northern part of the NVZ [52,53]. On the other hand, researchers that considered also geological data provided lower values for the Icelandic spreading direction, such as De Mets et al. [48], who provided a value of N104° E for the whole Iceland considering both GPS and geological data. From the plate velocity model of [48], Hjartardóttir et al. [13] calculated a value of N106° E for the NVZ. Finally, Bonali et al. [9,10,54] proposed a N103–108° E range, after completing an extensive UAV-based survey and conducting a major data collection campaign within Holocene units at the ThFS, located immediately west of the KFS.

3. Methods and Materials

3.1. Remote Sensing

Our work has been mainly focused on updating and classifying a major fracture set provided by Hjartardottir et al. [1], where all fractures were mapped using digitalised aerial photographs, without distinction between faults and extension fractures. We used aerial photos, satellite images and field surveys to assess the categories of brittle structures and define their geometry and kinematics. Aerial photos were obtained from Loftmyndir Inc. (Reykjavík, Iceland), with a resolution of 0.5–1 m/pixel, compared with aerial photos from Samsýn Inc. (0.5 m/pixel) and satellite images from the US/Japan ASTER project (15 m/pixel). All the considered aerial photographs were more recent than the latest Krafla event (1975–1984).

In order to analyse the rift architecture, we considered structures affecting both Post-LGM and Pre-LGM/LGM units as a unique dataset, because available information does not allow to assess which structures in the older units have been active also in the Holocene: such a classification would require a more detailed and extensive field survey on each single fracture, as demonstrated by Tibaldi et al. [55], who observed active fractures affecting a LGM hyaloclastite in the NW sector of the KFS. All the fractures have been classified as extension fractures, normal faults, eruptive fissures and caldera faults, also considering the geological map of the NVZ at a 1:100,000 scale [31]. To perform the classification, we used the above-cited materials, also with the aid of satellite images, the 30-m JAXA AW3D Digital Elevation Model and the shaded view of the high-resolution DSM from Loftmyndir Inc (https://www.map.is/base/ (accessed on 15 January 2021)). Normal faults were recognized and distinguished from extension fractures thanks to the presence on the DSM and on aerial photos of the shaded or better-lit slopes, which allowed also to distinguish between the E-dipping and W-dipping faults, respectively (Figure 2a,b). Extension fractures, instead, are expected to form by normal stress or fluid pressures and to open in a direction parallel to the minimum compressive principal stress (that is tensile near the surface), without any clear evidence of the shear components. Normal faults are excluded from this definition [56]; in fact, extension fractures do not show any well-lit slope or vertical offset.

In some cases, the presence of eruptive fissures could be directly identified on high-resolution aerial photos thanks to the recognition of volcanic deposits emplaced along the same fractures, whereas in other cases they were traced based on some morphometric parameters of related eruptive centres: the elongation of the cone base, the elongation of the crater and the alignment of cones were considered parallel to the strike of the feeding fracture, as summarised in Tibaldi and Bonali [57]. Finally, caldera faults were recognized on aerial photos with the aid of the DSM and the geological map, and were not considered in the detailed analysis of the present work.

3.2. Field Data Collection

In addition to the overall mapping and classification of all the structures in the KFS, three areas of the rift were surveyed in the field to a greater detail, so as to collect structural measurements along both the extension fractures and normal faults (Figure 2c,d). Structures were classified as normal faults when they showed a continuous vertical offset >0.50 m, whereas they were considered extension fractures when they were characterized by a vertical component <0.50 m, including both structures with a pure extensional opening and those with a lateral component.

At the extension fractures, we collected the local azimuth, amount of opening and opening direction where piercing points were detectable. In total, we collected 4086 measurements from a total of 1362 structural stations where piercing points were detectable, and 556 azimuth and dilation measurements from 278 sites, where piercing points were not visible. The net direction and amount of opening were quantified by measuring, respectively, the strike and the length of the line connecting the two piercing points (Figure 2c). Wherever piercing points were not observable, we measured the dilation amount orthog-

onally to the extension fracture walls. In order to measure the dilation amount, we used a tape or a laser rangefinder. To avoid the effect of erosion and gravity, we measured the dilation amount in the lower portions of the fractures, and only where fracture walls were clearly visible. In fact, sedimentation, erosion and weathering can cause a widening of the fracture on the surface, leading to possible overestimation of the amount of opening [10].

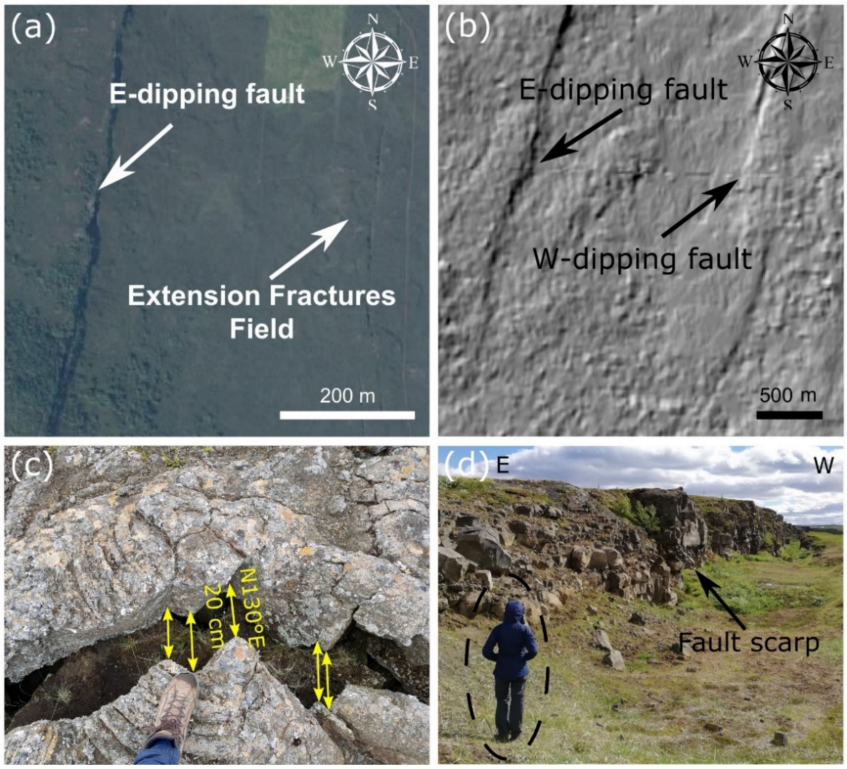

Figure 2. (**a**) Aerial photos with an E-dipping fault on the left, highlighted by the presence of a continuous shaded scarp, and an extension fracture field on the right (aerial photos available at www.map.is (accessed on 15 January 2021)); (**b**) sight of a graben in the northern part of the rift, identified thanks to the shading on the 30-m-resolution DEM; (**c**) example of extension fractures measured in the field, with visible piercing points; (**d**) example of W-dipping normal faults, where vertical offset values were measured in the field. Person for scale.

Along normal faults, we collected a total of 653 vertical offset values at intervals of 50 m. Where the scarps were in the order of meters, we used a tape or a laser rangefinder, whereas in the case of higher scarps, we used GPS measurements, calculating the difference in elevation between the two blocks.

3.3. Data Analysis

The azimuth and length of each mapped structure were calculated in a GIS environment (ArcMap v.10.6), together with the X and Y coordinates of the mean point, enabling to correlate these parameters and to analyse their possible variations in space. Moreover, we counted the number of structures along 97, N106° E-striking transects, each spaced 1 km in a N–S direction, to quantify the structure density variation along the rift. Along each transect, we also measured the rift width, considering the distance between the easternmost and the westernmost structure, and the average spacing. These analyses were carried out considering all types of structures at first, and then distinguishing between all the subsets (extension fractures, normal faults and eruptive fissures).

In the three field surveyed areas, we analysed all the collected data to check whether the different measured parameters showed correlations or spatial variations. Starting from the local azimuth and the opening direction values, it was possible to calculate the

lateral component of motion present in each structural site, to include this parameter in the analysis. Finally, we cumulated the dilation values along three transects, one for each area, striking N106° E, considering both extension fractures and normal faults, to calculate and compare the stretch values in three different sectors of the rift and with other rift zones in Iceland.

4. Results

4.1. Fracture Geometry

In the KFS, a total of 20,483 structures were recognized and classified as normal faults (8353—40.8%), extension fractures (11,807—57.6%) and eruptive fissures (296—1.5%) (Figure 3a). Of the remaining 27 structures, 8 were identified as caldera rim faults, whereas the very few remaining fractures were not classified, due to uncertainty on the available DEM and aerial photos.

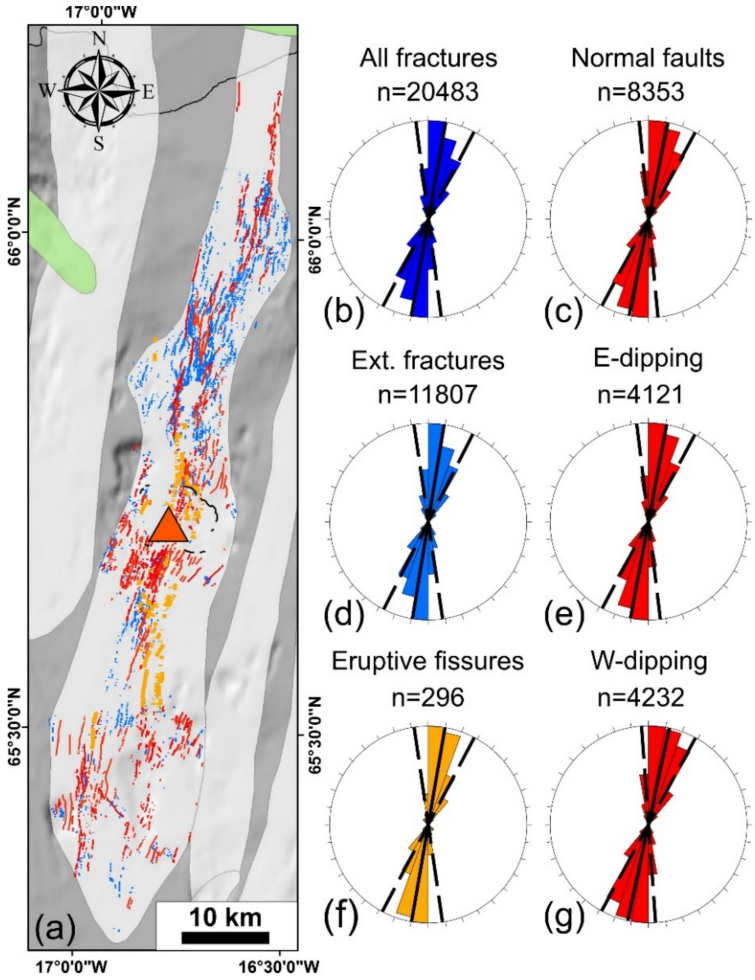

Figure 3. (**a**) Map representing all the structures in the KFS and the location of central volcanoes in this sector of the NVZ. Rose diagrams show the strike of (**b**) all KFS structures, (**c**) normal faults, (**d**) extension fractures, (**e**) E-dipping normal faults, (**f**) eruptive fissures and (**g**) W-dipping normal faults. The continuous black lines in the rose diagrams represent the average values, whereas dashed lines represent the standard deviation.

At a general level, fractures strike mostly N-S and NNE-SSW, with a peak between N0 and 10° E, an average of N10.1° E and a standard deviation (SD) of 17.5° (Figures 3b and 4a). The longest structure has a length of 4571.8 m, whereas the length average is 63.5 m, with a SD of 151.4 m (Figure 5a).

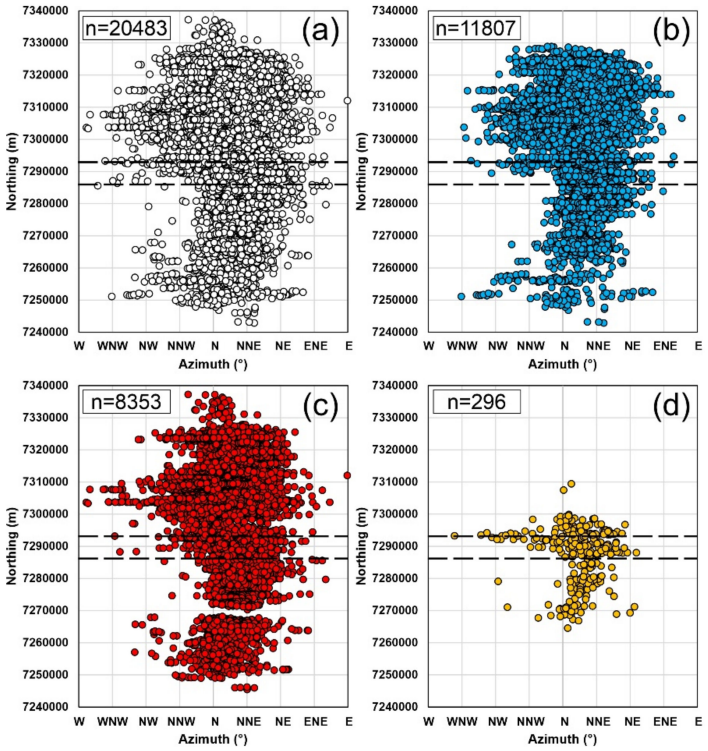

Figure 4. Graphs showing the strike values for the whole fractures set (**a**), extension fractures (**b**), normal faults (**c**) and eruptive fissures (**d**) subsets, with respect to the north. The northing is reported in the WGS84-UTM Zone 28N reference system. Black dashed lines show the location of the Krafla caldera.

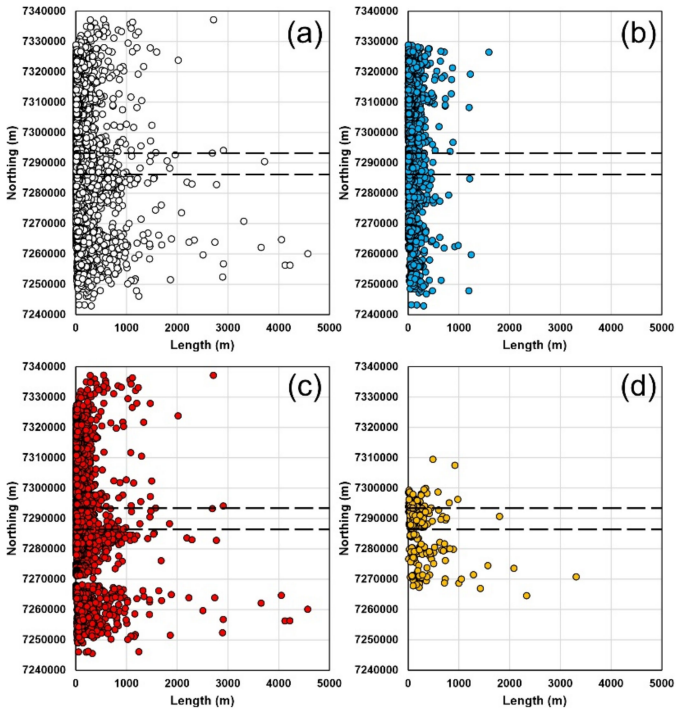

Figure 5. Graphs showing length values for the whole fractures set (**a**), extension fractures (**b**), normal faults (**c**) and eruptive fissures (**d**) subsets with respect to the north. The northing is reported in the WGS84-UTM Zone 28N reference system. Black dashed lines show the location of the Krafla caldera.

Regarding extension fractures, strike values are between NNW-SSE and NE-SW, with a peak between N0 and 10° E, an average of N9.3° E and a SD of 17.7° (Figure 3d). The maximum length is 1592.8 m with an average value of 44.3 m and a SD of 65.8 m (Figure 5b). Normal faults strike mostly N0–10° E, with an average of N11.4° E and a SD of 16.9° (Figure 3c). They reach the greatest lengths within the whole rift, with an average length value of 84 m and a SD of 203.9 m (Figure 5c). As far as normal faults are concerned, E-dipping ones mostly have a N-S strike, with a peak between N0 and 10° E, whereas W-dipping ones strike mainly NNE-SSW, with a peak between N0 and 20° E (Figure 3e,g). Finally, eruptive fissures present a prevalent N–S strike, with most values between N0 and 10° E, an average of N9.8° E and a SD of 18.1° (Figure 3f). They show a maximum and an average length of 3309.1 m and 219.2 m, respectively (Figure 5d).

Furthermore, strike and length values were related to the UTM X and Y coordinates (WGS84-UTM zone 28N). At a general level, by considering the whole set of fractures (Figure 4a), it is possible to observe that data distribution covers an about 100-km-long area, and that in the northern part of the rift, the azimuth values present a greater range than in the southern part, except for its southernmost part, which seems to be represented by extension fractures (Figure 4b). Additionally, it can be noticed that this range abruptly changes north of the Y coordinate 7,290,000, corresponding to the central caldera. This observation is also confirmed for the extension fractures set (Figure 4b) and normal faults (Figure 4c); the N-S areal coverage of the extension fractures is slightly lower than the normal fault set. South of this latitude, strike values of all types of structures tend to rotate in an anti-clockwise direction going southward, reaching a mostly N-S orientation. Regarding eruptive fissures, they are strongly limited to a N-S direction, covering an area as long as 46 km, showing the majority of data in the N-NNE range, with a broader range of values just north of the caldera centre (Figure 4d).

Regarding structure length, for the whole set of fractures (Figure 5a), we have observed the greater values in the central and southern part of the rift; the greatest values are reached by normal faults in the southern part (Figure 5c), where also eruptive fissures reach their greatest values (Figure 5d). Instead, extension fractures length values are constant across the whole rift, reaching the greatest values in the northern-central and southern part (Figure 5b).

In Figures 6 and 7, the strike and length, respectively, of the fractures and faults were related to the X coordinates (WGS84-UTM zone 28N). Regarding the strike values, considering the whole set of fractures (Figure 6a), the range is greater in the central part, near the X coordinate value 420,000, also corresponding to the Krafla caldera longitude, and decreases moving towards E and W to values included between NW and NE; towards the W, the decrease is more evident. Values between NNW and NNE are generally always represented. Such a pattern also can be noticed for the extension fractures and normal faults subsets (Figure 6b,c). Eruptive fissures (Figure 6d) are mostly located in the central part and the majority of the data show a strike between N and NE.

Regarding fracture length, in Figure 7a, the greatest values are in the western part of the rift, decreasing eastward. Most data show a length <1000 m. This pattern is also typical of the normal fault set (Figure 7c), whereas extension fractures show a majority of data with a length <500 m, and the longest values to the E (Figure 7b). Eruptive fissures show a majority of data with a length <500 m, with the maximum value in the W sector of the rift (Figure 7d).

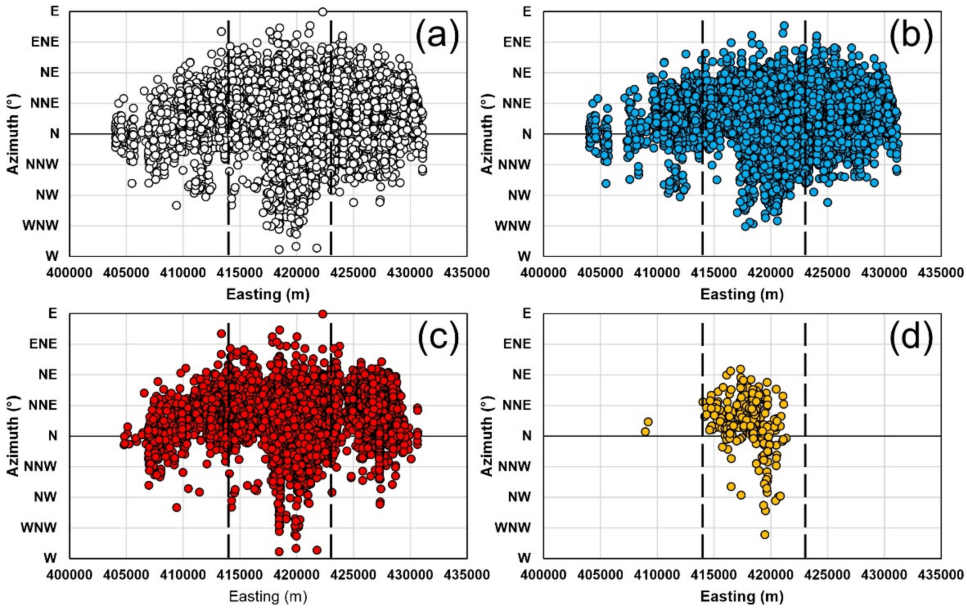

Figure 6. Graphs showing the azimuth values for the whole fractures set (**a**), extension fractures (**b**), normal faults (**c**) and eruptive fissures (**d**) subsets with respect to the east. The easting is reported in the WGS84-UTM Zone 28N reference system. Black dashed lines show the location of the Krafla caldera.

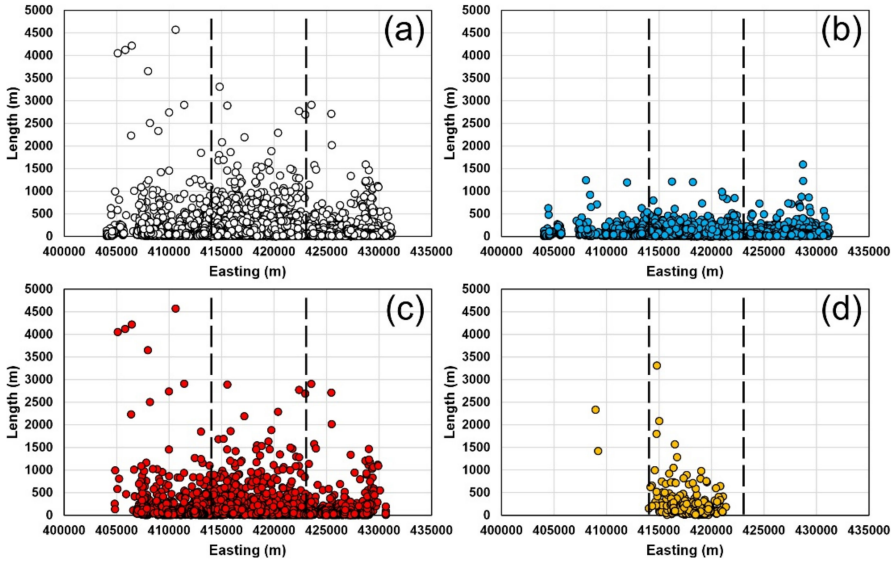

Figure 7. Graphs showing the length values for the whole fractures set (**a**), extension fractures (**b**), normal faults (**c**) and eruptive fissures (**d**) subsets with respect to the east. The easting is reported in the WGS84-UTM Zone 28N reference system. Black dashed lines show the location of the Krafla caldera.

In Figure 8, the strike and length of all the datasets were related, showing that the greatest lengths are associated with the N-S-oriented fractures, with strikes between N0 and 10° E (Figure 8a). Generally, longer structures (all sets) are in the N-NE range; the longest are mainly represented by normal faults and eruptive fissures with a similar relation between the azimuth and length as observed above (Figure 8c,d). The extension fracture set shows a similar pattern but with a shorter length (Figure 8b).

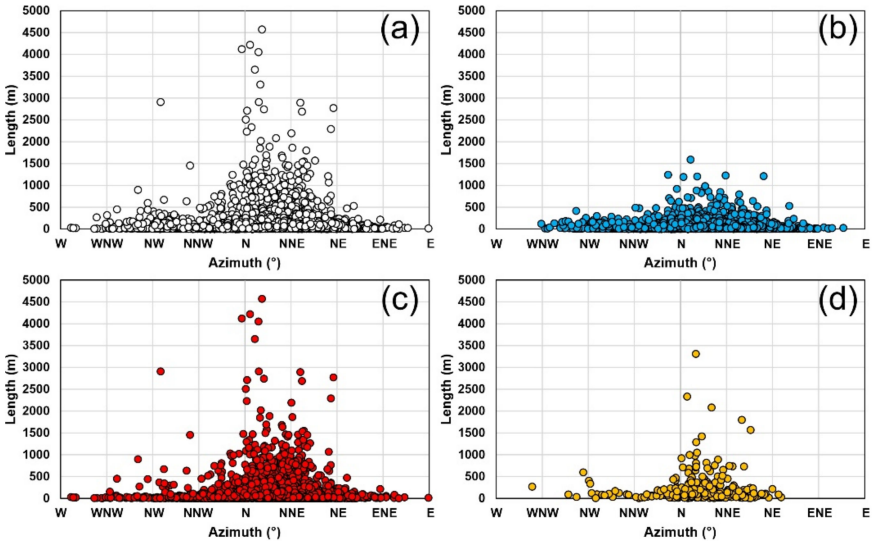

Figure 8. Graphs showing the relation between the strike and length of (**a**) all structures, (**b**) extension fractures, (**c**) normal faults and (**d**) eruptive fissures.

4.2. Fracture Density and Spacing

In order to detect fracture density variation, we traced 97 transects, striking N106° E, spaced 1 km from each other and parallel to the average spreading direction of the region [13]. Along each transect, we counted the number of intersecting fractures, first considering them all (Figure 9), then distinguishing between extension fractures (Figure 10), normal faults (Figure 11) and eruptive fissures (Figure 12). For each dataset we also measured the width of the fractured area, namely, the distance between the easternmost and the westernmost structure intersecting each transect, and the average spacing. The latter was calculated with the ratio width/number of structures, considering both the rift width (Figure 9c) and the width of the fractured area obtained considering only a specific type of structure. In Figure 10c, the width was calculated considering only extension fractures, whereas in Figures 11c and 12c we considered only normal faults and eruptive fissures, respectively; therefore, these values are not representative of the width of the whole rift. Finally, for the normal fault dataset, we also counted the number of E- and W-dipping faults intersecting each transect.

Regarding the whole dataset, the highest number of intersecting structures is observed at transect 34, where up to 50 structures were counted (Figure 9b). In the northernmost sector of the rift, the number of structures is in the range 0–6 north of transect 10. South of this transect, a gradual increase can be noticed up to the maximum at transect 34. Moving southward, the number of structures decreases to transect 51. This decrease corresponds to a section of the rift where historical lava flows crop out (between transects 35 and 52), covering older structures and reducing the frequency values. At transects 54, 55 and 56, south of the caldera, another peak can be observed, with values up to 44. Further south, the number of fractures decreases gradually, showing another smaller peak at transect 74, with 28 intersecting structures. Except for this peak, values remain in the range 4–28 up to transect 88, reaching values <6 in the southernmost transects. The rift width (considering all types of fractures) presents a range between 0 and 4.7 km north of transect 4, decreasing to <1 km between transects 5 and 10. Going southward, the rift width increases, reaching a maximum of 17.9 km at transect 58, south of the caldera. Further south, another peak, up to 17.4 km, can be observed at transect 75, with values always greater than 8 km between transects 72 and 88. In the southernmost sector of the rift, the width gradually decreases (Figure 9c). The average spacing thus appears greater in the northernmost part of the rift, with a maximum of 2.3 km at transect 1. Going southward, the spacing decreases to transect 5, staying in a range of 0.15–0.56 km up to transect 41. Further south, we can observe a slow

but gradual increase in the average spacing value, which reaches two peaks at transect 70 (1.55 km) and 80 (1.54 km), both in the southernmost sector of the KFS (Figure 9d).

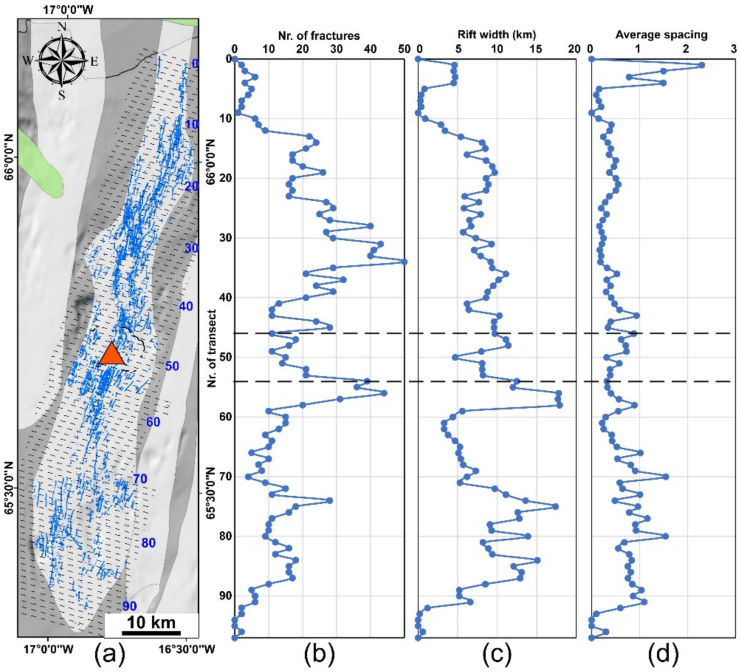

Figure 9. (**a**) Map representing all the structures of the KFS and the location of the central volcano. Black dashed lines show the N106° E-striking transects. Graphs showing (**b**) the number of total structures, (**c**) rift width and (**d**) the average spacing measured along the transects considering the whole structures. Black dashed lines in the graphs show the location of the Krafla caldera.

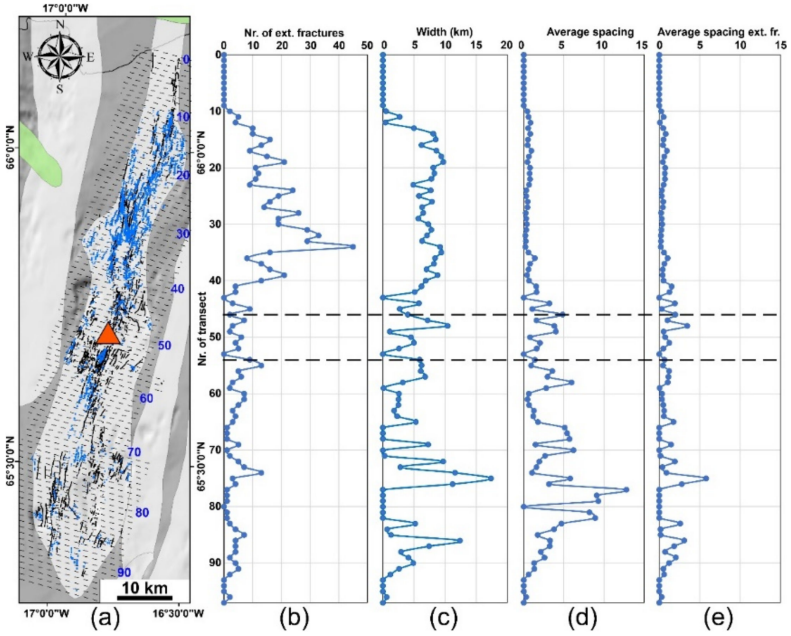

Figure 10. (**a**) Map representing extension fractures in the KFS, highlighted in blue. Black dashed lines show the N106° E-striking transects. Graphs showing (**b**) the number of extension fractures, (**c**) the rift width, (**d**) the average spacing considering the rift width shown in Figure 9c and (**e**) the average spacing considering the rift width shown in this figure, measured along the transects considering only extension fractures. Black dashed lines in the graphs show the location of the Krafla caldera.

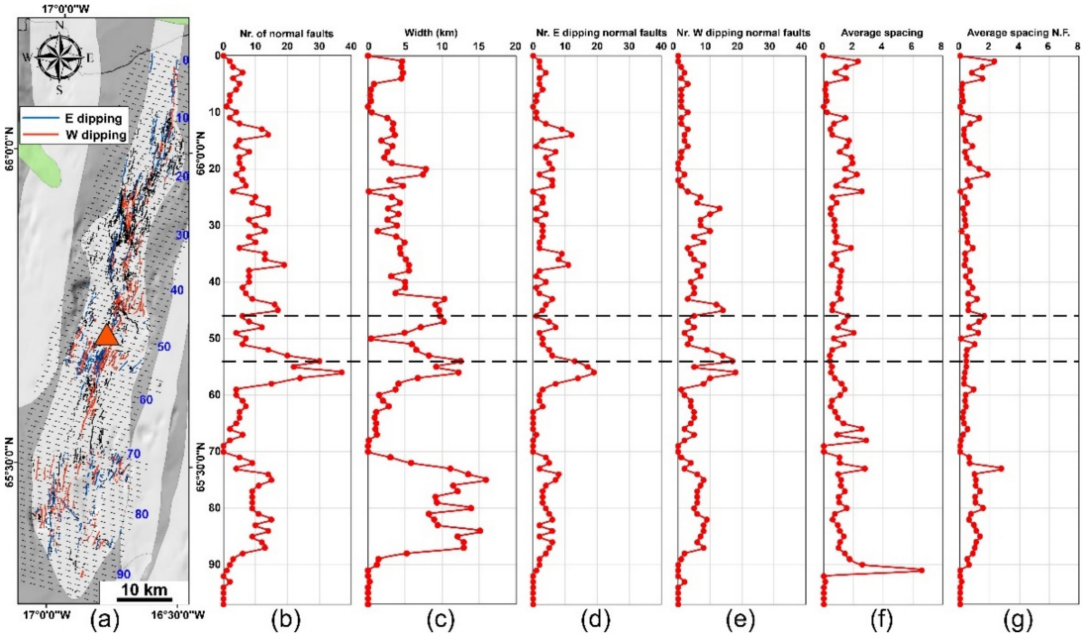

Figure 11. (**a**) Map representing normal faults in the KFS; E-dipping faults are shown in blue, W-dipping faults are shown in red. Black dashed lines show the N106° E-striking transects. Graphs showing (**b**) the number of normal faults, (**c**) the rift width, (**d**) the number of E-dipping normal faults, (**e**) the number of W-dipping normal faults, (**f**) the average spacing considering the rift width in Figure 9c and (**g**) the average spacing considering the rift width shown in this figure, measured along the transects considering only normal faults. Black dashed lines in the graphs show the location of the Krafla caldera.

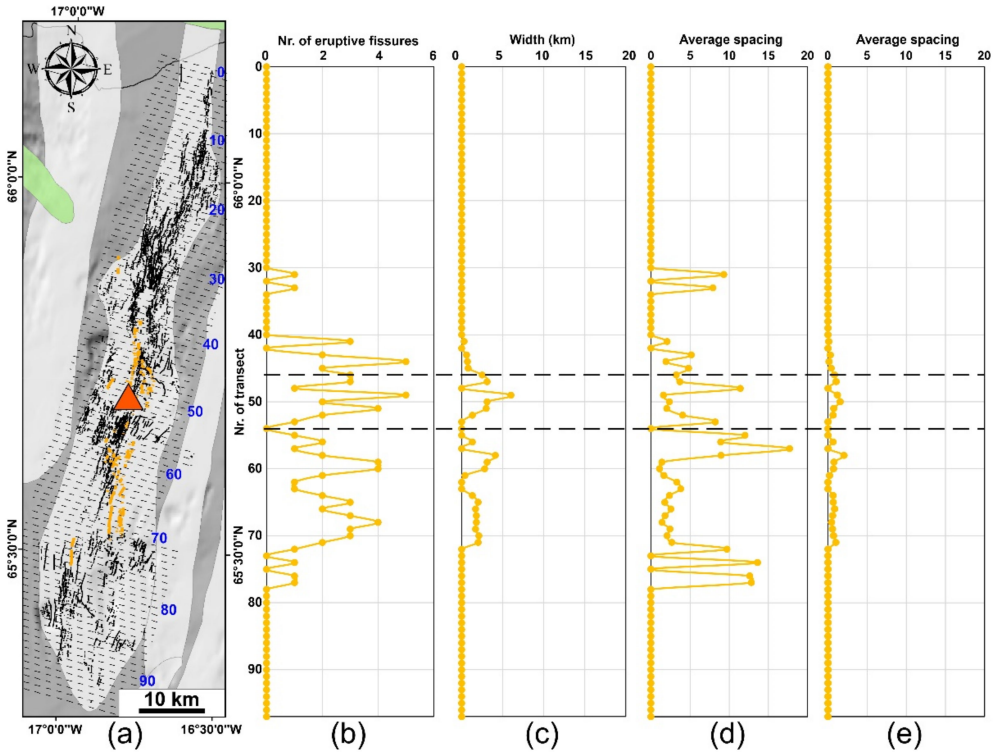

Figure 12. (**a**) Map representing eruptive fissures in the KFS, highlighted in yellow. Black dashed lines show the N106° E-striking transects. Graphs showing (**b**) the number of eruptive fissures, (**c**) the rift width, (**d**) the average spacing considering the rift width in Figure 9c and (**e**) the average spacing considering the rift width shown in this figure, measured along the transects considering only eruptive fissures. Black dashed lines in the graphs show the location of the Krafla caldera.

Regarding extension fractures, their number is null in the northernmost part up to transect 9, whereas south of it we can observe a gradual steady increase, culminating in the maximum value of 45 at transect 34. Further south, an abrupt decrease in the number of extension fractures is observed, with values always <13 (Figure 10b). The width of the fractured area (considering only extension fractures) is quite constant between transects 13 and 42, staying in a range of 5 and 9.7 km, whereas it shows continuous ups and downs going further south, reaching a maximum of 17.4 km at transect 75. In the southernmost sector, another peak can be observed, up to 12.4 km at transect 86 (Figure 10c). The average spacing was calculated considering the area width, for both the rift width and only the extension fractures area width. In the first case, we observe values <1 km up to transect 35. South of it, values increase, reaching a maximum of 12.8 km at transect 77, and decreasing in the southernmost part of the rift (Figure 10d). In the second graph, we can notice a similar pattern north of the caldera, whereas south of it values are smaller, consistently with the smaller width values obtained considering only extension fractures. The maximum of 5.8 km is reached at transect 75, where also the maximum rift width is reached (Figure 10e). Generally, the average spacing is greater in the central and southern part.

With regard to normal faults, the number of structures shows a gradual increase, starting from the northernmost transect and going southward, with three minor peaks: at transect 14 (where a value of 14 faults is reached), at transect 37 (up to 19 faults) and at transect 45 (up to 17 faults). The maximum of 37 is reached at transect 56 (Figure 11b), south of the caldera. At this transect, the maximum value also is reached for both the E- (19) and W-dipping (18) normal faults (Figure 11d,e). Focusing on the dip direction of the faults, E-dipping normal faults are prevalent north of transect 23, whereas between transect 23 and the caldera, W-dipping faults are prevalent. South of the maximum peak, W-dipping faults are prevalent up to transect 69, where the total value of faults decreases to 0. Further south, another relative increase in the total number of faults is observed between transects 74 and 87, in the southernmost part of the rift, where a plateau can be noticed, with values in the range 9–12, and an almost equal distribution between the E- and W-dipping faults. This part of the rift (transects 73–87) is also characterized by the maximum width of the faulted area, reaching a maximum of 15.9 km (Figure 11c). Other smaller peaks can be observed south of the caldera, at transects 54–56 (up to 12.5 km), and north of it, between transects 43 and 47 (up to 10.3 km). More to the north, the width is always <7.5 km. The two graphs showing average spacing, obtained as explained above, are very similar in the northern part of the rift, showing a peak with values up to 2.3 km at transects 1–4. Values decrease to 0 km between transects 5 and 10, increasing again between transects 11 and 21. More to the south, values decrease up to the southernmost part of the rift, where the maximum values are reached (6.6 km at transect 91 considering the whole dataset, and 2.77 km at transect 73 considering only the normal faults) (Figure 11f,g).

Finally, eruptive fissures can be observed only in the central part of the rift, between transects 31 and 77, whereas they disappear moving away from Krafla volcano (Figure 12b). The number of eruptive fissures reaches a maximum (5) in the proximity of the caldera, at transects 44 and 49, and decreases going northward and southward. The same pattern can be observed considering the width of the fractured area, whose maximum is reached in the caldera, at transect 49, with a value of 6 km; however, except for this transect, the width is always less than 4.1 km (Figure 12c). The average spacing considering the whole dataset of structures reaches a value up to 17.7 km at transect 57, due to the limited number of eruptive fissures if compared to the extension fractures and normal faults in the rift (Figure 12d). On the contrary, considering just the eruptive fissure dataset, the average spacing shows a maximum value of 2.05 km at transect 58, with a decrease going northward and southward (Figure 12e).

4.3. Fracture Kinematics and Dilation

In the field, we collected data of the extension fracture local strike, opening direction and amount of opening at 1362 different sites (Figure 13a), for a total of 4086 structural

measurements along fractures affecting the Post-LGM units. Such sites are mainly located in three areas, two of which north of the caldera and one south of it (Figure 13b–d). It is worth noting that, in 278 sites where the opening direction was not recognizable, we collected only the strike and dilation amount of the extension fractures, reaching a total of 4642 structural measurements at 1640 different sites. Along the normal faults, we collected 653 vertical offset values in order to estimate the stretch over the three areas. Opening direction values present a wide range, between N39° and 148° E, with an average value of N99.5° E (SD 14.8°) (Figure 13a). In the northern area, the opening directions have a range between N48.5° and 148.5° E, with an average of N103.2° E and a SD of 15.7° (Figure 13e). In the sector situated north of the caldera, the range is the greatest (N39°–148° E), with an average of N98.7° E and a SD of 14.7° (Figure 13f). Finally, in the southern sector, values are comprised between N78.5° and 138.5° E, with an average of N107.7° E and a SD of 12.4° (Figure 13g). In Figure 14a, we show the relation between the opening direction and northing: the greatest range is in correspondence with the sector located north of the caldera, whereas in the northern part of the rift and south of the caldera, it decreases. In the southern part, we can observe a clockwise rotation of the opening direction values going northward, towards the central caldera. Regarding easting, we notice that the range of values is greatest in the central part of the rift, decreasing towards the E and W (Figure 14c).

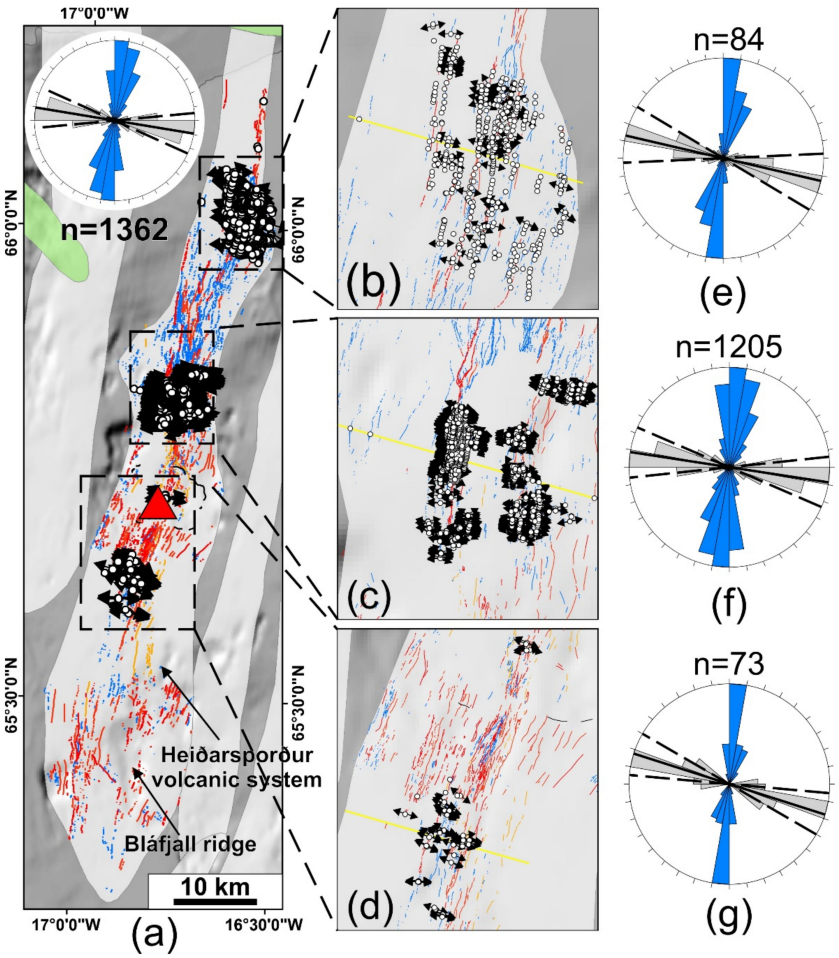

Figure 13. (**a**) Map of the KFS, same scale and north of Figure 9a, showing as white dots the location of all the structural measurements collected in the field. Rose diagram shows the 1362 opening directions (grey) and the local azimuth values (blue) of the extension fractures. The opening directions are represented by black diverging arrows. The three areas are shown more in detail in (**b**–**d**), with their respective rose diagrams in (**e**–**g**). Yellow lines in (**b**–**d**) represent the three N106° E-oriented transects; the continuous black lines in the rose diagrams represent the average values; dashed lines represent the standard deviation.

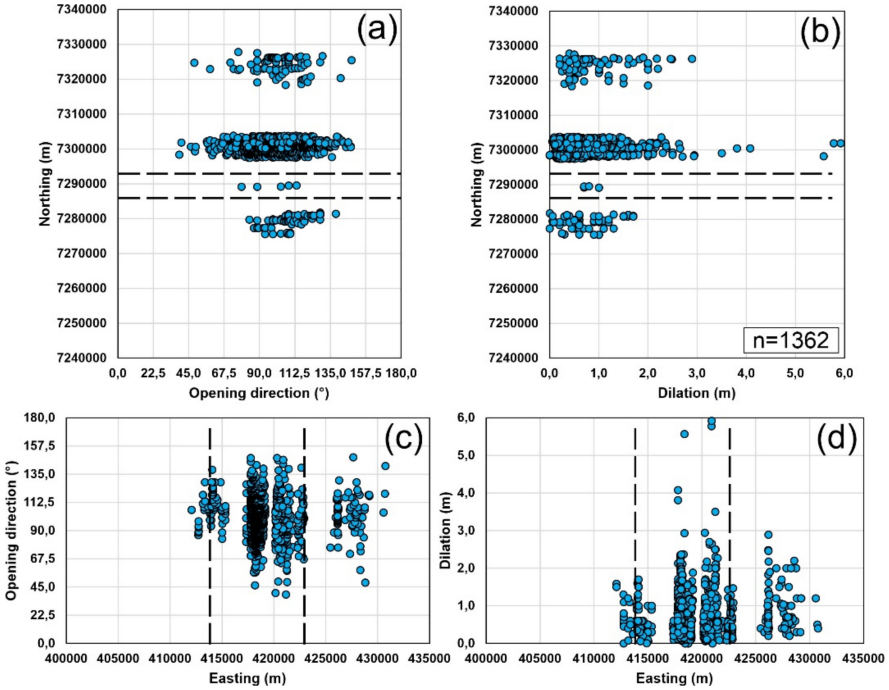

Figure 14. (**a**) Graph relating the opening direction vs. northing. (**b**) Graph relating dilation vs. northing. (**c**) Graph relating the opening direction vs. easting. (**d**) Graph relating dilation vs. easting. Coordinates are in the WGS84-UTM Zone 28N reference system. Black dashed lines show the location of the Krafla caldera.

As far as net dilation is concerned, we found a maximum value of 5.9 m, with an average of 0.7 m (SD 0.5 m). With respect to northing, the greatest values are in the central sector, and in the northern part of the rift we notice greater values than in the southern sector (Figure 14b). In the E–W direction, the maximum values are reached at the centre of the rift, decreasing going towards its sides (Figure 14d). Dilation values tend to be greater for the opening direction values between N90° and 113° E (Figure 15b).

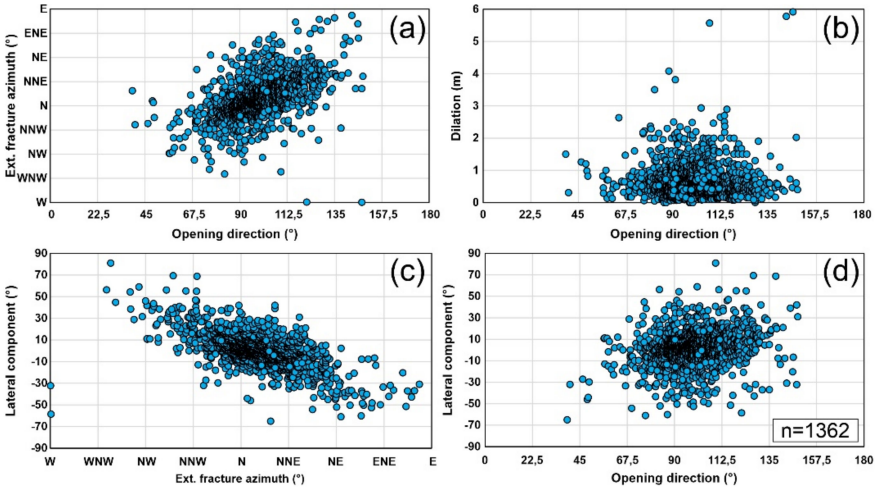

Figure 15. (**a**) Graph relating the opening direction vs. fracture azimuth. (**b**) Graph relating the opening direction vs. dilation. (**c**) Graph relating the fracture azimuth vs. lateral component. (**d**) Graph relating the opening direction vs. lateral component.

Local strike values are in the range N270.2° W–N84.1° E, with an average value of N8.2° E and a SD of 19.7° (rose diagram in Figure 13a). We have related these values to the opening directions, showing that a clockwise rotation of the latter corresponds to an

overall clockwise rotation of local strike (Figure 15a). Considering the average values of the opening direction and fracture strike in the rift, we thus obtained an overall small right-lateral component of motion of 1.5° (Figure 13a). Actually, we have analysed the results more in detail, distinguishing between pure extension fractures (when the local lateral component was <5°) and fractures with a lateral (right or left) component of motion (when the local lateral component was >5°), finding out that 453 fractures are characterized by pure extension, whereas 497 fractures have a right-lateral component and 412 a left lateral component (Figure 15c,d). Right-lateral component values reach a maximum of 81°, while left-lateral ones have a maximum of 65° (Figure 15c,d). With a clockwise rotation of the fracture strike, lateral components tend to switch from right-lateral to left-lateral (Figure 15c), whereas with a clockwise rotation of the opening directions the lateral component behaviour is the opposite (Figure 15d).

Finally, in order to measure the stretch along the rift, we traced three transects, one for each area, oriented in the overall regional spreading direction (N106° E) [13] (Figure 13b–d). Along these transects, the dilation values were added up, considering both extension fractures and normal faults: at the extension fractures, we measured dilation as explained in the methodology section, whereas at normal faults, we calculated the heave starting from the measured vertical offset, considering a fault dip of 75°. All transects have a length of 9.75 km, and the resulting cumulative dilation is 13.87 m in the northern area, 27.50 m in the central area and 14.70 m south of the caldera. Considering these resulting values, we thus obtained a stretch of 1.0014 in the north, 1.0028 in the central part and 1.0015 in the southern sector.

5. Discussion

5.1. Rift Architecture

We have performed an in-depth reconstruction of the architecture of the KFS through the detailed mapping of all its structures, as well as an assessment of their geometry, distribution and kinematics; we have also distinguished between extension fractures, normal faults and eruptive fissures. This represents an outstanding result, especially considering the width of the KFS, which extends onshore for a length of 97 km and reaches a maximum width of 17.9 km south of the central caldera (Figure 9c). Moreover, we have quantified the strike and length of all KFS structures: normal faults are longer than extension fractures, suggesting that, along the rift, the latter might represent an earlier stage of evolution before developing into faults. This has also been observed in the field, where some normal faults turn into extension fractures at their tips. On the other hand, normal faults can further develop by propagating both vertically and laterally through linkage and nucleation, and this has the effect of increasing their vertical offset and length [58,59]. Regarding the relation between the length and orientation of structures, it is worth highlighting that all structures with a N-S and NNE-SSW orientation have greater lengths (Figure 8): being perpendicular to the regional spreading direction (N106°E) [13], the development of these structures is facilitated by regional tectonics, more so than for those with different orientations.

Considering the distribution of normal faults vs. extension fractures, our data show that the former are prevalent in the southern part of the rift, whereas the latter dominate in its northernmost sector (Figures 10b and 11b). This distribution of the structures has also been observed at the adjacent ThFS [7,9], suggesting a northward propagation of both rifts, as observed also by Saemundsson [60]; in fact, normal faults show a clear decrease in length and frequency moving northward (Figure 5c). Considering all the above, it can be argued that the northernmost sector represents an earlier stage of rift formation, where faults still have not fully developed. Regarding structure distribution, it is worth highlighting that, within transects 35–52, the decrease in fracture frequency can be influenced by the presence of historic lava flows (<870 AD [31]), covering the older fractures and causing an underestimation of the result. This occurs also south of the central volcano, within transects 58–72, where historical and prehistorical lavas (<2.9 ka BP [31]) crop out.

Eruptive fissures are only found within a distance of 20 km north of the central volcano, and 30 km south of it, whereas they disappear further north or south (Figure 12b). This can be interpreted as a consequence of the lateral shallow propagation of dykes from the central volcano, which tend to deepen with distance [46], inducing surface deformation represented mainly by dry extension fractures. This is coherent with other volcanic systems in Iceland (e.g., the Askja Fissure Swarm) [61], and also with the observations made during historic rifting episodes, when eruptive fissures were detected at the surface in the first 6–7 km from the central volcano, whereas extension fractures were observed as far away as tens of kilometres [14,47]. Eruptive fissures further away can also be explained by lateral feeding, as had occurred in the Holuhraun eruption in 2014, where the event started with a dyke propagating from the Bárðarbunga central volcano and reaching the surface when the seismicity reached north of the Vatnajökull glacier, triggering the eruption when the dyke was about 48 km long [62].

The propagation of eruptive fissures at a greater distance south of the central volcano than in the northern part of the rift might just be a coincidence, or it may be explained by the presence of an additional deep magmatic source in this region, as suggested by Saemundsson [33]. Supporting this hypothesis, chemical analyses by Jónasson [63] have shown that all the eruptive fissures situated in the south-eastern sector of the rift are part of the Heiðarsporður volcanic system, already considered as a separate volcanic system by Sæmundsson [25], together with the Bláfjall ridge more to the south; this additional magma source could also influence the width of the rift, and would help explain its widening, as observed in the southernmost sector, where the Bláfjall ridge is located (Figures 9c and 13a). The greater width in this sector could be explained also by the presence of Pre-LGM units affected by fractures (the age of the units is from Saemundsson et al. [31]; Figure 16a); they could have simply recorded a longer time of extensional deformation and, eventually, moved apart by rifting events. This southernmost sector is affected mostly by normal faults (Figure 16b) and extension fractures (Figure 16c), whereas eruptive fissures are not present (Figure 16d). Furthermore, Pre-LGM/LGM units crop out also in correspondence of the caldera, in the central part of the rift, where another increase in rift width can be observed (Figure 16a).

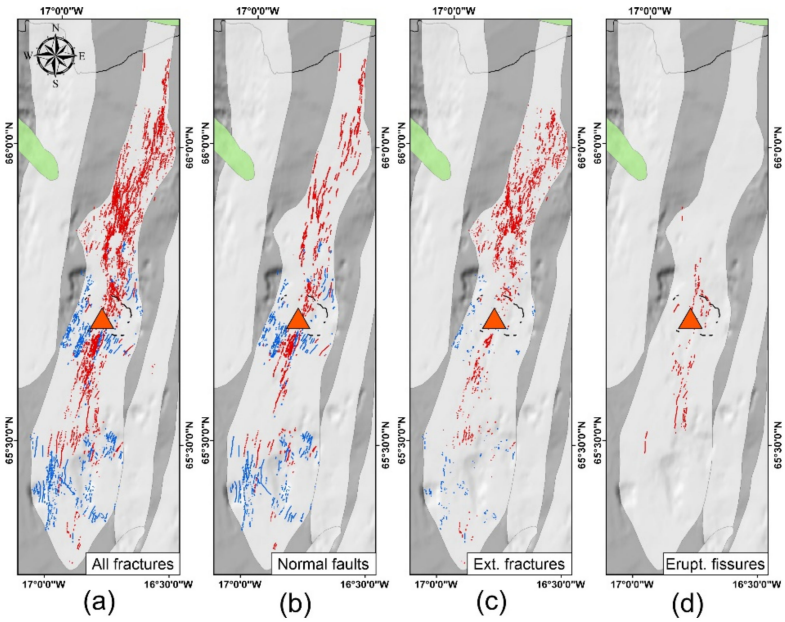

Figure 16. Maps showing (**a**) all fractures, (**b**) normal faults, (**c**) extension fractures and (**d**) eruptive fissures, distinguishing between those affecting Post-LGM units (in red) and those affecting Pre-LGM/LGM units (in blue). The ages of the units are from Saemundsson et al. [31].

Fractures affecting the Pre-LGM units seem, in general, longer than those affecting the Post-LGM units: this can be simply due to the fact that older faults had more time to develop and thus became longer.

The extension fractures peak observed at transect 34 mentioned above, characterized by a decrease in the number of normal faults, is situated at the intersection with the HFF prolongation, as observed also by Hjartardottir et al. [1]. This feature has also been noted in the ThFS by Tibaldi et al. [5,8] and Bonali et al. [9], who suggested the prolongation of the HFF as a buried fault further to the south-east. The hypothesis made on the continuation of the HFF as far as the KFS, which is also suggested by Hjartardottir et al. [13], is based on three observations: (i) the migration of earthquakes along the HFF that was observed for a few hours during the dyke intrusion of January 1978 in the KFS; (ii) the widening of the KFS central graben; and (iii) the increase in fracture density at the intersection between the KFS and the HFF prolongation, as also confirmed by our work. The different propagation pattern of eruptive fissures north and south from the central volcano could have been influenced by the presence of the HFF as well, which may reduce their northward propagation. Moreover, we observed a greater range in the azimuth values for both the extension fractures and normal faults where the HFF prolongation intersects the KFS (Figure 4a–c), with more structures oriented NNW-SSE and NW-SE, if compared to what is observed in the other sectors of the rift. This is another similarity with the ThFS, where the presence of the HFF is considered as responsible for the anti-clockwise rotation of structures [7,64], and of a greater range of azimuth values within a distance of 500 m from the HFF [5].

The range of structure strike increases in the southernmost part of the rift: this can be linked to the presence of a WNW-oriented belt acting as a transform zone, as interpreted by Hjartardottir et al. [1]. In fact, these authors observed the presence of several WNW-oriented fractures in the southernmost part of the KFS; this fracture system extends to the northernmost sector of the Kverkfjoll Fissure Swarm, thus forming a WNW-oriented belt across the NVZ. Due to its geometry, crossing the southernmost part of the KFS and the northernmost part of the Kverkfjoll Fissure Swarm, this belt has been interpreted as a transfer zone, which shifts the spreading of the NVZ westward. On the other hand, from east to west, the greater range of fracture strikes is observed along the axial part of the rift (Figure 6), thus suggesting a greater structural complexity than in the lateral sector, where deformation is more coherent with regional tectonics.

5.2. Rift Extension Rate

The cumulative dilation and stretch values were quantified in the northernmost part of the rift and just north and south of the caldera structure, passing through Holocene units (Figure 13b–d). The greatest total dilation value, which is 27.5 m, is reached in the central area, a few kilometres north of the caldera, where the most recent lava flows could have hidden some fractures, causing an underestimation of the resulting value. This value is very similar to the one calculated by Dauteuil et al. [65], who estimated a total extension of 30 m just north of the 1984 Krafla lava flow. Moving to the northernmost part of the rift and just south of the caldera, according to our data the total dilation value is about 14 m.

Furthermore, the stretch ratio that we calculated for the same area, 1.003, is in the same order of magnitude of Dauteuil et al. [65], who obtained a stretch ratio of 1.009. To the north and to the south, stretch values are about 1.001 and 1.002, respectively. A higher value than 1.003 has been calculated in the KFS in a previous research by Bonali et al. [4], but since this value takes into account also older units, it cannot be considered for comparison; the same goes for the stretch value of 1.036–1.046 from Paquet et al. [66], which has been calculated across the Tertiary Alftafjördur dyke swarm, thus describing a deformation that lasted at least 1 Ma. We suggest that the stretch value calculated in the present work, and by Dauteuil et al. [65], can be representative of tectonic and magma forces working together, also considering that in the central area of the rift some eruptive fissures are present. Assuming an age of 11.5 $\pm$ 0.5 ka BP for the post-LGM lava units [31], we obtained an

extension rate of 2.4 ± 0.7 mm/yr in the central area, and 1.2 ± 0.7 mm/yr in the northern part. Regarding the southern area, it is mostly affected by younger lava flows, which have covered faults and fractures. Our transect is the only one that intersects old-enough lavas to possibly provide a meaningful result, as it crosses through three small lava units of uncertain ages. The results from the southern profile are therefore more uncertain than the profiles north of Krafla.

All these rates are much slower than the GPS velocity field measured after the 1975–1984 rifting/dyking period (3–4.5 cm/yr) [45], suggesting, in agreement with Bonali et al. [4], that the latter values are not representative for the long-term deformation field of the KFS. From another point of view, our values represent a fraction of the extension of the whole NVZ, which corresponds to 1.8–2.3 cm/yr [48,67].

5.3. Rift Kinematics and Spreading Direction

Focusing on the kinematics of extension fractures, the collected data suggest an overall average (av.) spreading direction of N99.5° E and a SD of 14.8°. Considering the three different areas, from north to south, the av. values are N103.2° E +/−15.7°, N98.7° E +/−14.7°and N107.7° E +/−12.4°, respectively. Thus, the av. values obtained considering the whole area and the central one are almost similar, and are both slightly lower than the spreading range values given in the literature, which are N106° E [13] and N112° E [18] for the whole NVZ, and N109° E and N115° E for the northern part of the NVZ [52,53]. Our spreading directions in the northern and southern area are closer to the values that take into account geological data covering a larger time window, such as those of Hjartardóttir et al. [13] (N106° E) and of DeMets et al. [48] (N104° E), although the latter refer to the whole Iceland, whereas they are instead slightly rotated anti-clockwise with respect to spreading directions based only on GPS data [18,52,53]. Furthermore, our data indicate a more pronounced anti-clockwise rotation of the spreading direction just north of the caldera border and the central volcano, where eruptive fissures are present and where shallow dyking is reported in the literature [55].

The overall fracture strike is suggested to be orthogonal to the spreading vector range discussed in the above section; in fact, longer and thus more developed fractures (in terms of extension fractures and normal faults) and eruptive fissures show an azimuth between N-S and NNE-SSW (Figure 8), confirming the observation made by Hjartardóttir et al. [13]. Furthermore, we investigated the presence of strike-slip components of motion along the extension fractures, with a predominance of right-lateral with respect to left-lateral components of motion, which is coherent with what has been observed in the neighbouring ThFS, where 854 fractures (52%) out of 1633 were characterized by a right-lateral component [7]. Another similarity with the ThFS pertains to the relation with opening directions; in fact, also in the ThFS, a shift from the left-lateral to right-lateral components has been observed alongside a clockwise rotation of the opening direction values [7]. Recent research efforts support the hypothesis that such lateral components can be induced by local perturbations exerted by dyking at shallow depths, as shown for the 2014–2015 Bárðarbunga dyking event [68], and as suggested in the ThFS [7–10] and by field data by Bonali et al. [4] in the KFS. Furthermore, as suggested by Einarsson and Brandsdóttir [15], magma was injected during the July 1978 event at a total distance of 30 km from the caldera into the northern fracture swarm through lateral dyke propagation. Other dykes propagated even further into the fissure swarm, such as in January 1976 (60 km) and January 1978 (45 km) [14,69].

5.4. General Considerations

The approach used in the present work, based on a detailed survey of all the structures of a rift and their differentiation as normal faults, extension fractures and volcanic fissures, was proven effective in assessing the possible propagation direction of a rift. This result is based on an evaluation of the frequency of faults vs. extension fractures, assuming that the latter might develop earlier than the former [3]. This approach can be applied as

an alternative to the evaluation of rift propagation based on the reconstruction of fault slip profiles. This considers that single faults develop in the direction where their slip profile tapers out [70]. Both methods have been tested at the ThFS rift [6,8], giving the same result of a preferential northward-directed rift propagation. However, we believe that, on one hand, the slip profile methodology is very time consuming, as it implies the continuous measurement of the offset along each fault for all the structures of a rift, but on the other hand it allows for a better definition of the propagation direction of single structures within the general trend of a rift. At the ThFS, in fact, it was documented that single faults can develop outward from the central volcano, suggesting that they might be related to the outward propagation of dykes from the magma chamber [8]. This double outward propagation of faults has been observed also at the Ado'Ale volcano, located in the Ethiopian Rift [71], implying that this model can be of wider relevance. We thus suggest that, in the future, an analysis of fault slip profiles at the Krafla rift should be carried out, in order to assess if, also at this rift, faults are propagating outward from the central volcano.

The finding of a preferential northward-directed development of both the ThFS and the Krafla rift is relevant for the evaluation of the geodynamics of northern Iceland, as it might suggest that the whole North Volcanic Zone is propagating in that direction. This is important also at the local scale, because it hints at the possibility that new fractures may preferentially develop in the northern part of the rifts, or existing fractures may lengthen northward.

With regard to the dilation amount and dilation directions, the differences between our data, which pertain to the Holocene time span and GPS-based ones [18,52,53], which are related to much shorter time intervals, in the order of years, highlight how much a deformation field can be perturbed as a consequence of a transient event. The Krafla rift, in fact, has been affected by a major intrusive episode, which happened between 1975 and 1984, known as the "Krafla Fires", during which around 20 dykes were injected along the rift [44]. We thus assume that caution should be exerted when using GPS data for geodynamic studies in rift zones where recent dyking has taken place. A more reliable assessment of dilation direction and amount should instead be derived from data related to Holocene structures, which bear information over a longer time span. Similarly, attention should be paid to the presence of huge volcano edifices or calderas; our data show that the dilation amount and rift spreading direction change in correspondence to the Krafla caldera system, with rotation of the dilation direction also in the order of ten degrees.

Finally, the discovery of transcurrent components of motion along the fractures of the Krafla rift increases awareness of this phenomenon. This has been partly explained as induced by the obliquity of some fractures in comparison with the regional tectonic stress field, but in part it is independent from this process. Recently, some authors have suggested that transcurrent components of slip at volcanotectonic rifts may derive from the lateral (horizontal) propagation of magma along dykes [55,62,68,72]. The presence of strike-slip components at the fractures of the Krafla rift, which are supposed to be linked to shallow dyke injection, shed further light on the frequent occurrence of this process.

6. Conclusions

We have studied the geometry, kinematics and offset amount of the structures that form the active, N-S-trending KFS, mapping and analysing all the extension fractures, normal faults and eruptive fissures of the rift by remote sensing and field survey. Furthermore, in three areas distributed in the northern, central and southern part of the rift, we have collected detailed structural measurements through extensive field surveys along the post-LGM extension fractures and normal faults, obtaining the following conclusions:

(1) Regarding structure geometry, normal faults are longer than extension fractures. This suggests that, along the rift, extension fractures might represent an earlier stage of evolution before developing into faults. Normal faults are prevalent in the southern part of the rift, whereas extension fractures dominate in the northernmost sector.

This structure distribution has also been observed at the adjacent ThFS, suggesting a northward propagation of both rifts; in fact, normal faults show a clear decrease in length and frequency going northward. Structures with N-S and NNE-SSW orientations are longer: being perpendicular to the regional spreading direction (N106° E), their development is facilitated by regional tectonics, more so than for those with different orientations.

(2) Eruptive fissures are present only within a distance of 20 km north of the Krafla volcano, and 30 km south of it. This can be interpreted as a consequence of the lateral shallow propagation of dykes from the central volcano, which tend to deepen with distance, causing surface deformation represented mainly by dry extension fractures.

(3) The extension fractures peak observed at transect 34, characterized by a decrease in the number of normal faults, is situated where the KFS intersects with the possible Húsavík-Flatey Fault prolongation. Moreover, we observed a greater range in the azimuth values for both the extension fractures and normal faults, always at the intersection with the HFF propagation.

(4) The greatest total dilation value of 27.5 m was reached in the central area, a few kilometres north of the caldera. In the northernmost part of the rift and just south of the caldera, our data show that the total dilation value is about 14 m. Assuming the age of 11.5 $\pm$ 0.5 ka BP for the post-LGM lava units, we obtain an extension rate of 2.4 $\pm$ 0.7 mm/yr in the central area, and 1.2 $\pm$ 0.7 mm/yr in the northern part.

(5) The collected data indicate an overall average spreading direction of N99.5° E. Considering the three different surveyed areas, from north to south, the average values are N103.2° E +/−15.7°, N98.7° E +/−14.7°and N107.7° E +/−12.4°, respectively. The average values considering the whole area and the central one are almost similar, and are both slightly lower than the spreading range values given in the literature, i.e., N106° E and N112° E for the whole NVZ, and N109° E and N115° E for the northern part of the NVZ. Our spreading directions in the northern and southern area are closer to the values that take into account geological data covering a wider time span, whereas they are instead slightly rotated anti-clockwise with respect to the spreading directions based only on GPS data.

(6) Finally, we have observed the presence of strike-slip components of motion along the extension fractures: 453 fractures (33%) are characterized by pure extension, 497 fractures (37%) present right-lateral component and 412 (30%) present a left-lateral component. On one side, these components are related to the rotation of fracture strike, and thus to a control by regional tectonics. On the other side, such lateral components can be induced by local perturbations exerted by dyking at shallow depths.

Author Contributions: Conceptualization and writing of the paper is from N.C., F.L.B., A.T. and F.P.M.; field data collection is from F.L.B., N.C., E.R., V.R. and S.B.; Á.R.H. and P.E. provided the fractures dataset and contributed to the manuscript; N.C. improved the fracture classification with the help of F.L.B. and A.T. All authors have read and agreed to the published version of the manuscript.

Funding: This study was conducted in the framework of the International Lithosphere Program—Task Force II (Leader A. Tibaldi).

Data Availability Statement: The data presented in this study are available on request from the corresponding author.

Acknowledgments: Three anonymous reviewers are acknowledged for their useful comments on an early version of the manuscript.

Conflicts of Interest: The authors declare no conflict of interest.

References

1. Hjartardóttir, Á.R.; Einarsson, P.; Magnusdóttir, S.; Bjornsdóttir, P.; Brandsdóttir, B. Fracture systems of the Northern Volcanic Rift Zone, Iceland: An onshore part of the Mid-Atlantic plate boundary. In *Magmatic Rifting and Active Volcanism*; Wright, T.J., Ayele, A., Ferguson, D.J., Kidane, T., Vye-Brown, C., Eds.; Geological Society of London: London, UK, 2016; Volume 420, pp. 297–314.
2. Angelier, J.; Bergerat, F.; Dauteuil, O.; Villemin, T. Effective tension-shear relationships in extensional fissure swarms, axial rift zone of northeastern Iceland. *J. Struct. Geol.* **1997**, *19*, 673–685. [CrossRef]
3. Acocella, V.; Gudmundsson, A.; Funiciello, R. Interaction and linkage of extension fractures and normal faults: Examples from the rift zone of Iceland. *J. Struct. Geol.* **2000**, *22*, 1233–1246. [CrossRef]
4. Bonali, F.L.; Tibaldi, A.; Corti, N.; Fallati, L.; Russo, E. Reconstruction of Late Pleistocene-Holocene Deformation through Massive Data Collection at Krafla Rift (NE Iceland) Owing to Drone-Based Structure-from-Motion Photogrammetry. *Appl. Sci.* **2020**, *10*, 6759. [CrossRef]
5. Tibaldi, A.; Bonali, F.; Einarsson, P.; Hjartardottir, A.R.; Mariotto, F.P. Partitioning of Holocene kinematics and interaction between the Theistareykir Fissure Swarm and the Husavik-Flatey Fault, North Iceland. *J. Struct. Geol.* **2016**, *83*, 134–155. [CrossRef]
6. Tibaldi, A.; Bonali, F.; Mariotto, F.P.; Russo, E.; Tenti, L.R. The development of divergent margins: Insights from the North Volcanic Zone, Iceland. *Earth Planet. Sci. Lett.* **2019**, *509*, 1–8. [CrossRef]
7. Tibaldi, A.; Bonali, F.L.; Mariotto, F.P.; Corti, N.; Russo, E.; Einarsson, P.; Hjartardóttir, Á.R. Rifting Kinematics Produced by Magmatic and Tectonic Stresses in the North Volcanic Zone of Iceland. *Front. Earth Sci.* **2020**, *8*, 174. [CrossRef]
8. Tibaldi, A.; Corti, N.; Bonali, F.; Mariotto, F.P.; Russo, E. Along-rift propagation of Pleistocene-Holocene faults from a central volcano. *J. Struct. Geol.* **2020**, *141*, 104201. [CrossRef]
9. Bonali, F.; Tibaldi, A.; Mariotto, F.P.; Saviano, D.; Meloni, A.; Sajovitz, P. Geometry, oblique kinematics and extensional strain variation along a diverging plate boundary: The example of the northern Theistareykir Fissure Swarm, NE Iceland. *Tectonophysics* **2019**, *756*, 57–72. [CrossRef]
10. Bonali, F.; Tibaldi, A.; Marchese, F.; Fallati, L.; Russo, E.; Corselli, C.; Savini, A. UAV-based surveying in volcano-tectonics: An example from the Iceland rift. *J. Struct. Geol.* **2019**, *121*, 46–64. [CrossRef]
11. Einarsson, P.; Saemundsson, K. Earthquake epicentres 1982–1985 and volcanic systems in Iceland (map). In *Í Hlutarins Eðli, Festschrift for Thorbjörn Sigurgeirsson*; Sigfússon, T.I., Ed.; Menningarsjóður: Reykjavík, Iceland, 1987.
12. Magnúsdóttir, S.; Brandsdóttir, B. Tectonics of the Þeistareykir fissure swarm. *Jökull* **2011**, *61*, 65–79.
13. Hjartardóttir, Á.R.; Einarsson, P.; Bramham, E.; Wright, T.J. The Krafla fissure swarm, Iceland, and its formation by rifting events. *Bull. Volcanol.* **2012**, *74*, 2139–2153. [CrossRef]
14. Buck, W.R.; Einarsson, P.; Brandsdóttir, B. Tectonic stress and magma chamber size as controls on dike propagation: Constraints from the 1975–1984 Krafla rifting episode. *J. Geophys. Res. Solid Earth* **2006**, *111*, B12. [CrossRef]
15. Einarsson, P.; Brandsdóttir, B. Seismological evidence for lateral magma intrusion during the July 1978 deflation of the Krafla volcano in NE-Iceland. *J. Geophys.* **1980**, *47*, 160–165.
16. Lyakhovsky, V.; Segev, A.; Schattner, U.; Weinberger, R. Deformation and seismicity associated with continental rift zones propagating toward continental margins. *Geochem. Geophys. Geosystems* **2012**, *13*, 01012. [CrossRef]
17. Keir, D.; Ebinger, C.J.; Stuart, G.W.; Daly, E.; Ayele, A. Strain accommodation by magmatism and faulting as rifting proceeds to breakup: Seismicity of the northern Ethiopian rift. *J. Geophys. Res. Space Phys.* **2006**, *111*, 05314. [CrossRef]
18. Drouin, V.; Sigmundsson, F.; Ófeigsson, B.G.; Hreinsdóttir, S.; Sturkell, E.; Einarsson, P. Deformation in the Northern Volcanic Zone of Iceland 2008–2014: An interplay of tectonic, magmatic, and glacial isostatic deformation. *J. Geophys. Res. Solid Earth* **2017**, *122*, 3158–3178. [CrossRef]
19. Sigmundsson, F.; Einarsson, P.; Hjartardóttir, Á.R.; Drouin, V.; Jónsdóttir, K.; Árnadóttir, T.; Geirsson, H.; Hreinsdóttir, S.; Li, S.; Ófeigsson, B.G. Geodynamics of Iceland and the signatures of plate spreading. *J. Volcanol. Geotherm. Res.* **2020**, *391*, 106436. [CrossRef]
20. Gudmundsson, A. Dynamics of Volcanic Systems in Iceland: Example of Tectonism and Volcanism at Juxtaposed Hot Spot and Mid-Ocean Ridge Systems. *Annu. Rev. Earth Planet. Sci.* **2000**, *28*, 107–140. [CrossRef]
21. Einarsson, P. Plate boundaries, rifts and transforms in Iceland. *Jökull* **2008**, *58*, 35–58.
22. Mjelde, R.; Digranes, P.; Van Schaack, M.; Shimamura, H.; Kodaira, S.; Naess, O.; Sørenes, N.; Vågnes, E.; Shiobara, H. Crustal structure of the outer Vøring Plateau, offshore Norway, from ocean bottom seismic and gravity data. *J. Geophys. Res. Space Phys.* **2001**, *106*, 6769–6791. [CrossRef]
23. Jacoby, W.; Gudmundsson, M.T. Hotspot Iceland: An introduction. *J. Geodyn.* **2007**, *43*, 1–5. [CrossRef]
24. Jakobsdóttir, S.S.; Roberts, M.J.; Guðmundsson, G.B.; Geirsson, H.; Slunga, R. Earthquake swarms at Upptyppingar, North-east Iceland: A sign of magma intrusion? *Stud. Geophys. Geod.* **2008**, *52*, 513–528. [CrossRef]
25. Saemundsson, K. Evolution of the axial rifting zone in northern Iceland and the Tjörnes fracture zone. *Geol. Soc. Am. Bull.* **1974**, *85*, 495–504. [CrossRef]
26. Gudmundsson, A. Infrastructure and evolution of ocean-ridge discontinuities in Iceland. *J. Geodyn.* **2007**, *43*, 6–29. [CrossRef]
27. Bergerat, F.; Angelier, J. Immature and mature transform zones near a hot spot: The South Iceland Seismic Zone and the Tjörnes Fracture Zone (Iceland). *Tectonophysics* **2008**, *447*, 142–154. [CrossRef]

28. Stefánsson, R.; Gudmundsson, G.B.; Halldorsson, P. Tjörnes fracture zone. New and old seismic evidences for the link between the North Iceland rift zone and the Mid-Atlantic ridge. *Tectonophysics* **2008**, *447*, 117–126. [CrossRef]
29. Wolfe, C.J.; Bjarnason, I.T.; Vandecar, J.C.; Solomon, S.C. Seismic structure of the Iceland mantle plume. *Nat. Cell Biol.* **1997**, *385*, 245–247. [CrossRef]
30. Hjartardóttir, Á.R.; Einarsson, P.; Björgvinsdóttir, S.G. Fissure swarms and fracture systems within the Western Volcanic Zone, Iceland—Effects of spreading rates. *J. Struct. Geol.* **2016**, *91*, 39–53. [CrossRef]
31. Saemundsson, K.; Hjartarson, A.; Kaldal, I.; Sigurgeirsson, M.A.; Kristinsson, S.G.; Vikingsson, S. *Geological map of the Northern Volcanic Zone, Iceland. Northern Part 1: 100.000*; Iceland GeoSurvey and Landsvirkjun: Reykjavik, Iceland, 2012.
32. Mattsson, H.B.; Höskuldsson, Á. Contemporaneous phreatomagmatic and effusive activity along the Hverfjall eruptive fissure, north Iceland: Eruption chronology and resulting deposits. *J. Volcanol. Geotherm. Res.* **2011**, *201*, 241–252. [CrossRef]
33. Sæmundsson, K. Geology of the Krafla system. In *The Natural History of Lake Myvatn*; Gardarson, A., Einarsson, Á., Eds.; Icelandic Natural History Society: Reykjavik, Iceland, 1991; pp. 24–95.
34. Rooyakkers, S.M.; Stix, J.; Berlo, K.; Barker, S.J. Emplacement of unusual rhyolitic to basaltic ignimbrites during collapse of a basalt-dominated caldera: The Halarauður eruption, Krafla (Iceland). *GSA Bull.* **2020**, *132*, 1881–1902. [CrossRef]
35. Jónasson, K. Rhyolite volcanism in the Krafla central volcano, north-east Iceland. *Bull. Volcanol.* **1994**, *56*, 516–528. [CrossRef]
36. Einarsson, P. S-wave shadows in the Krafla Caldera in NE-Iceland, evidence for a magma chamber in the crust. *Bull. Volcanol.* **1978**, *41*, 187–195. [CrossRef]
37. Tryggvason, E. Multiple magma reservoirs in a rift zone volcano: Ground deformation and magma transport during the September 1984 eruption of Krafla, Iceland. *J. Volcanol. Geotherm. Res.* **1986**, *28*, 1–44. [CrossRef]
38. Grönvold, K.; Halldórsson, S.A.; Sigurðsson, G.; Sverrisdóttir, G.; Óskarsson, N. Isotopic systematics of magma movement in the Krafla Central Volcano, North Iceland. In Proceedings of the Goldschmidt Conference, Vancouver, Canada, 13–18 July 2008; p. A331.
39. Björnsson, A.; Sæmundsson, K.; Einarsson, P.; Tryggvason, E.; Grönvold, K. Current rifting episode in north Iceland. *Nature* **1977**, *266*, 318–323. [CrossRef]
40. Sigmundsson, F.; Hooper, A.; Hreinsdóttir, S.; Vogfjörd, K.S.; Ófeigsson, B.G.; Heimisson, E.R.; Dumont, S.; Parks, M.; Spaans, K.; Gudmundsson, G.B.; et al. Segmented lateral dyke growth in a rifting event at Bárðarbunga volcanic system, Iceland. *Nature* **2015**, *517*, 191–195. [CrossRef] [PubMed]
41. Hjartardóttir, Á.R.; Einarsson, P.; Gudmundsson, M.T.; Högnadóttir, T. Fracture movements and graben subsidence during the 2014 Bárðarbunga dike intrusion in Iceland. *J. Volcanol. Geotherm. Res.* **2016**, *310*, 242–252. [CrossRef]
42. Einarsson, P. Earthquakes and present-day tectonism in Iceland. *Tectonophysics* **1991**, *189*, 261–279. [CrossRef]
43. Björnsson, A.; Johnsen, G.; Sigurdsson, S.; Thorbergsson, G.; Tryggvason, E. Rifting of the plate boundary in north Iceland 1975–1978. *J. Geophys. Res. Space Phys.* **1979**, *84*, 3029–3038. [CrossRef]
44. Tryggvason, E. Widening of the Krafla fissure swarm during the 1975–1981 volcano-tectonic episode. *Bull. Volcanol.* **1984**, *47*, 47–69. [CrossRef]
45. Hofton, M.A.; Foulger, G.R. Postrifting anelastic deformation around the spreading plate boundary, north Iceland: 1. Modeling of the 1987-1992 deformation field using a viscoelastic Earth structure. *J. Geophys. Res. Space Phys.* **1996**, *101*, 25403–25421. [CrossRef]
46. Hollingsworth, J.; Leprince, S.; Ayoub, F.; Avouac, J.-P. New constraints on dike injection and fault slip during the 1975-1984 Krafla rift crisis, NE Iceland. *J. Geophys. Res. Solid Earth* **2013**, *118*, 3707–3727. [CrossRef]
47. Einarsson, P. The volcanic unrest at Krafla 1975-89. In *Náttúra Mývatns*; Garðarsson, A., Einarsson, Á., Eds.; Hið íslenska náttúrufræðifélag: Reykjavík, Iceland, 1991; pp. 96–139.
48. DeMets, C.; Gordon, R.G.; Argus, D.F.; Stein, S. Effect of recent revisions to the geomagnetic reversal time scale on estimates of current plate motions. *Geophys. Res. Lett.* **1994**, *21*, 2191–2194. [CrossRef]
49. Saemundsson, K. Fissure swarms and central volcanoes of the neovolcanic zones of Iceland in Crustal evolution in northern Britain and adjacent regions. *Geol. J. Liverpool* **1978**, *10*, 415–432.
50. Heki, K.; Foulger, G.R.; Julian, B.R.; Jahn, C.H. Plate dynamics near divergent plate boundaries: Geophysical implications of post-rifting crustal deformation in NE Iceland. *J. Geophys. Res.* **1993**, *98*, 14279–14297. [CrossRef]
51. Sigmundsson, F. *Iceland Geodynamics, Crustal Deformation and Divergent Plate Tectonics*; Springer Science & Business Media: Chichester, UK, 2006.
52. Metzger, S.; Jónsson, S.; Geirsson, H. Locking depth and slip-rate of the Húsavík Flatey fault, North Iceland, derived from continuous GPS data 2006-2010. *Geophys. J. Int.* **2011**, *187*, 564–576. [CrossRef]
53. Metzger, S.; Jónsson, S.; Danielsen, G.; Hreinsdóttir, S.; Jouanne, F.; Giardini, D.; Villemin, T. Present kinematics of the Tjörnes Fracture Zone, North Iceland, from campaign and continuous GPS measurements. *Geophys. J. Int.* **2013**, *192*, 441–455. [CrossRef]
54. Bonali, F.L.; Corti, N.; Russo, E.; Marchese, F.; Fallati, L.; Pasquaré Mariotto, F.; Tibaldi, A. Commercial-UAV-based Structure from Motion for geological and geohazard studies. In *Building Knowledge for Geohazard Assessment and Management in the Caucasus and Other Orogenic Regions*; Bonali, F.L., Tsereteli, N., Pasquarè Mariotto, F., Eds.; NATO SPS Series; Springer: Berlin/Heidelberg, Germany, 2020.
55. Tibaldi, A.; Bonali, F.; Russo, E.; Fallati, L. Surface deformation and strike-slip faulting controlled by dyking and host rock lithology: A compendium from the Krafla Rift, Iceland. *J. Volcanol. Geotherm. Res.* **2020**, *395*, 106835. [CrossRef]
56. Gudmundsson, A. *Rock Fractures in Geological Processes*; Amsterdam University Press: Amsterdam, The Netherlands, 2011.

57. Tibaldi, A.; Bonali, F. Intra-arc and back-arc volcano-tectonics: Magma pathways at Holocene Alaska-Aleutian volcanoes. *Earth-Sci. Rev.* **2017**, *167*, 1–26. [CrossRef]
58. Cladouhos, T.T.; Marrett, R. Are fault growth and linkage models consistent with power-law distributions of fault lengths? *J. Struct. Geol.* **1996**, *18*, 281–293. [CrossRef]
59. Mansfield, C.; Cartwright, J. Fault growth by linkage: Observations and implications from analogue models. *J. Struct. Geol.* **2001**, *23*, 745–763. [CrossRef]
60. Sæmundsson, K. Outline of the geology of Iceland. *Jokull* **1979**, *29*, 7–28.
61. Hjartardóttir, Á.R.; Einarsson, P.; Sigurdsson, H. The fissure swarm of the Askja volcanic system along the divergent plate boundary of N Iceland. *Bull. Volcanol.* **2009**, *71*, 961–975. [CrossRef]
62. Ágústsdóttir, T.; Woods, J.; Greenfield, T.; Green, R.G.; White, R.S.; Winder, T.; Brandsdóttir, B.; Steinthórsson, S.; Soosalu, H. Strike-slip faulting during the 2014 Bárðarbunga-Holuhraun dike intrusion, central Iceland. *Geophys. Res. Lett.* **2016**, *43*, 1495–1503. [CrossRef]
63. Jónasson, K. Magmatic evolution of the Heiðarsporður ridge, NE-Iceland. *J. Volcanol. Geotherm. Res.* **2005**, *147*, 109–124. [CrossRef]
64. Tibaldi, A.; Bonali, F.L.; Mariotto, F.P.; Russo, E. Interplay between inherited rift faults and transcurrent structures: Insights from analogue models and field data from Iceland. *Glob. Planet. Chang.* **2018**, *171*, 88–109.
65. Dauteuil, O.; Angelier, J.; Bergerat, F.; Verrier, S.; Villemin, T. Deformation partitioning inside a fissure swarm of the northern Icelandic rift. *J. Struct. Geol.* **2001**, *23*, 1359–1372. [CrossRef]
66. Paquet, F.; Dauteuil, O.; Hallot, E.; Moreau, F. Tectonics and magma dynamics coupling in a dyke swarm of Iceland. *J. Struct. Geol.* **2007**, *29*, 1477–1493. [CrossRef]
67. Perlt, J.; Heinert, M.; Niemeier, W. The continental margin in Iceland—A snapshot derived from combined GPS networks. *Tectonophysics* **2008**, *447*, 155–166. [CrossRef]
68. Ruch, J.; Wang, T.; Xu, W.; Hensch, M.; Jónsson, S. Oblique rift opening revealed by reoccurring magma injection in central Iceland. *Nat. Commun.* **2016**, *7*, 12352. [CrossRef]
69. Wright, T.J.; Sigmundsson, F.; Pagli, C.; Belachew, M.; Hamling, I.J.; Brandsdóttir, B.; Keir, D.; Pedersen, R.; Ayele, A.; Ebinger, C.; et al. Geophysical constraints on the dynamics of spreading centres from rifting episodes on land. *Nat. Geosci.* **2012**, *5*, 242–250. [CrossRef]
70. Manighetti, I.; King, G.C.P.; Gaudemer, Y.; Scholz, C.H.; Doubre, C. Slip accumulation and lateral propagation of active normal faults in Afar. *J. Geophys. Res. Space Phys.* **2001**, *106*, 13667–13696. [CrossRef]
71. Dumont, S.; Klinger, Y.; Socquet, A.; Doubre, C.; Jacques, E. Magma influence on propagation of normal faults: Evidence from cumulative slip profiles along Dabbahu-Manda-Hararo rift segment (Afar, Ethiopia). *J. Struct. Geol.* **2017**, *95*, 48–59. [CrossRef]
72. Russo, E.; Tibaldi, A.; Waite, G.; Bonali, F.; Massin, F.; Farrell, J. Unraveling the complex deformation pattern at Yellowstone plateau through seismicity and fracture analysis. *Tectonophysics* **2020**, *778*, 228352. [CrossRef]